RSC Advances

PAPER

View Article Online
View Journal | View Issue

Cite this: *RSC Adv.*, 2026, **16**, 5941

Low-concentration cholesterol modification enhances *Clematis filamentosa* Dunn-derived extracellular vesicle-mediated macrophage polarization regulation for acute lung injury therapy

Guanglin Zhang,†[ab] Huadong Liang,†[b] Guanyan Zhang,[c] Changyao Chen,[b] Junjie Lai,[b] Hongjia Huang,[d] Liubing Hu,[d] Baiyin Yu,[ab] Xiang Li,[ab] Rong Zeng[c] and Jie Chen*[ab]

Acute lung injury (ALI) and its severe form, acute respiratory distress syndrome (ARDS), are characterized by an imbalance in M1/M2 macrophage polarization and disruption of the alveolar-capillary barrier. Although plant-derived extracellular vesicles (PEVs) hold therapeutic potential for immunomodulation, their clinical application is limited by poor stability and inefficient delivery. Here, we developed cholesterol-modified nanovesicles (CHOL@CDNVs) from *Clematis filamentosa* Dunn (CDNVs), a medicinal plant with documented anti-inflammatory properties. Using a thin-film hydration–extrusion method, low-concentration cholesterol modification enhanced the colloidal stability of the vesicles and increased macrophage uptake by 1.6-fold while preserving their ROS scavenging capacity. CHOL@CDNVs effectively suppressed M1 polarization and the secretion of TNF-α/IL-1β, while inducing M2 reprogramming. In an LPS-induced ALI mouse model, CHOL@CDNVs administration reduced pulmonary edema (37% lower wet/dry weight ratio) and fibrosis (67% reduction in collagen deposition) without inducing hepatotoxicity. These therapeutic effects were mediated by a shift from M1 to M2 macrophage polarization and the resolution of inflammatory properties. This study establishes cholesterol modification as a dual-functional strategy that simultaneously enhances the stability and immunoregulatory efficacy of plant-derived nanovesicles, offering a promising advance toward precision therapy for ALI/ARDS.

Received 19th November 2025
Accepted 9th January 2026

DOI: 10.1039/d5ra08928j

rsc.li/rsc-advances

1 Introduction

Acute lung injury (ALI) and its severe manifestation, acute respiratory distress syndrome (ARDS), are life-threatening conditions, pathologically characterized by a dysregulated inflammatory response, uncontrolled oxidative stress, disruption of the alveolar-capillary barrier, and consequent progressive hypoxemia.[1,2] Currently, the global management of ALI/ARDS remains largely supportive care, lacking targeted interventions that can substantially improve survival rates.[3] Moreover, the widely used corticosteroids are frequently associated with severe adverse effects.[4] A central pathogenic event in ALI/ARDS is the imbalance in macrophage M1/M2 polarization, a pivotal immunoregulatory process. This imbalance features hyperactivation of pro-inflammatory M1 macrophages, which exacerbate inflammation through a cytokine storm (*e.g.*, TNF-α, IL-1β), coupled with a deficiency in anti-inflammatory M2 macrophages, resulting in impaired tissue repair.[5–8] Accumulating evidence indicates that the dynamic regulation of macrophage polarization plays a central role in modulating alveolar-capillary barrier integrity, wherein the equilibrium between the M1 (pro-inflammatory) and M2 (pro-resolving) phenotypes dictates disease progression.[9–11] A hallmark of the pathological progression in ALI/ARDS is a vicious cycle in which persistent inflammatory stimuli drive macrophage overactivation. This amplifies inflammatory cascades and sustains a dominant M1 polarization state, which in turn exacerbates alveolar epithelial injury and pulmonary edema, ultimately leading to respiratory failure.[12,13] Given this central role, strategies aimed at reprogramming macrophages to reverse their pathogenic polarization state are emerging as a promising

[a]*Guangdong Province Key Lab of Utilization and Conservation of Food and Medicinal Resources in Northerrn Region, Shaoguan University, Shaoguan, Guangdong 512005, P. R. China*

[b]*School of Biology and Agriculture, Shaoguan University, Shaoguan, 512005, P. R. China. E-mail: maggiecj049@sgu.edu.cn*

[c]*Department of Materials Science and Engineering, College of Chemistry and Materials, Jinan University, Guangzhou, 510632, P. R. China*

[d]*College of Life Science and Technology, Jinan University, Guangzhou, 510632, P. R. China*

† Guanglin Zhang and Huadong Liang contributed equally to this work.

therapeutic avenue for severe pulmonary inflammatory disorders.

Extracellular vesicles (EVs) have recently garnered considerable attention as promising cell-free therapeutic nanomedicines, offering innovative alternatives for the treatment of ALI.[14] As cell-secreted, lipid-bilayer-enclosed nanoparticles, EVs play a fundamental role in intercellular communication.[15] Evidence has shown that Mammalian-derived EVs (MEVs) can effectively modulate macrophage phenotypes and their therapeutic potential has been validated in models of ALI.[16–18] However, the clinical translation of MEVs faces several challenges including limited yield, short half-life, and potential safety concerns such as tumorigenicity.[19] Given these limitations, plant-derived EVs (PEVs) are gaining increasing attention as viable alternatives. While sharing fundamental physicochemical similarities with MEVs, PEVs can also deliver a diverse array of endogenous bioactive compounds (*e.g.*, proteins, lipids, and nucleic acids) to target cells.[20] Compared to EVs from other sources, PEVs present distinct advantages, including high biocompatibility, low toxicity, minimal immunogenicity, as well as abundant source availability, cost-effectiveness, and excellent scalability.[21] Owing to their inherent anti-inflammatory and antioxidant properties, PEVs are positioned as compelling candidates for ALI intervention. For instance, PEVs derived from *Platycodon grandiflorum* mitigate ALI progression through the suppression of pro-inflammatory cytokines (TNF-α, IL-6) while enhancing anti-inflammatory IL-10 secretion, leading to the reprogramming of pulmonary macrophages toward reparative phenotypes.[22] Growing evidence underscores the therapeutic potential of PEVs from diverse botanical sources (*e.g.*, ginger, grape, broccoli, grapefruit, and *Artemisia annua*) in inflammatory diseases, largely attributed to their intrinsic anti-inflammatory and antioxidant activities.[23–25] Collectively, these findings underscore the translation potential of PEVs and pave the way for their further development as clinical intervention for ALI.

Clematis filamentosa Dunn, a perennial woody vine belonging to the genus *Clematis* (Ranunculaceae), is renowned in traditional medicine for its properties in clearing liver-heat, inducing tranquility, reducing blood pressure, and exerting meridian-activating analgesic effects.[26] While its stems and leaves have a history of use in herbal medicine, modern pharmacological investigations have substantiated a range of bioactivities, including cardiovascular protective, anti-inflammatory, antioxidant, and tissue-repair-promoting effects. These validated bioactive properties provide a strong rational for exploring its potential in treating inflammatory disease and promoting tissue regeneration.[27] Based on this foundation, the present study investigates extracellular vesicles derived from *Clematis filamentosa* Dunn (CDNVs) as a novel nanotherapeutic strategy for ALI. Despite their therapeutic potential, the clinical translation of natural PEVs such as CDNVs is often impeded by suboptimal delivery efficiency and structural instability, which lead to premature functional loss and thereby compromise therapeutic efficacy.[28,29] Therefore, enhancing the stability and delivery efficiency of PEVs constitutes a pivotal challenge that must be addressed to advance their clinical translation.

Cholesterol, a critical component of membrane systems, improves the structural integrity of lipid vesicles by increasing the rigidity of the lipid bilayer and facilitates delivery efficiency through lipid raft-mediated internalization pathways.[30] For instance, Zhuo *et al.* established that cholesterol-enriched exosomes can deliver siRNA directly into the cytoplasm *via* membrane fusion, leading to potent gene silencing.[31] It is important to note, however, that elevated cholesterol levels may promote protein–membrane interactions, consequently increasing the risk of rapid clearance from systemic circulation.[32] Despite this, low-concentration cholesterol modification offers a viable strategy to achieve an optimal balance between membrane stability and delivery efficiency. Herein, we developed a low-concentration cholesterol modification strategy for CDNVs. By anchoring cholesterol molecules into the CDNVs' lipid bilayer, we constructed an engineered system termed CHOL@CDNVs, which exhibits enhanced membrane stability and improved delivery capacity. To comprehensively assess its therapeutic efficacy, we employed both LPS-induced macrophage inflammation models and ALI animal models to systematically evaluate multifunctional effects, including the restoration of M1/M2 polarization balance, suppression of oxidative stress, and promotion of lung tissue regeneration. Collectively, these findings provide both valuable insights and a scalable engineering platform for advancing plant-derived vesicle-based therapies against ALI.

2 Materials and methods

2.1 Materials

Fresh leaf samples of *Clematis filamentosa* Dunn were collected from natural populations in Shixing County (GPS coordinates: 114.030414° N, 25.10987004° E), Guangdong Province, China, and authenticated by Prof. Zongli Hu. Cholesterol (CHOL), 2,2-diphenyl-1-picrylhydrazyl (DPPH), and polyethylene glycol (PEG 8000) were purchased from Macklin Biochemical Co., Ltd (Shanghai, China). Lipopolysaccharide (LPS), fluorescein-conjugated DHPE, chlorpromazine hydrochloride, and wortmannin were obtained from Sigma-Aldrich (St. Louis, MO, USA). Filipin III was sourced from MedChemExpress LLC (Monmouth Junction, NJ, USA). Recombinant murine IFN-γ was procured from PeproTech Inc. (Cranbury, NJ, USA). Tribromoethanol (1.25% solution for anesthesia) was acquired from Nanjing Aibei Biotechnology Co., Ltd (Nanjing, China). The BCA Protein Assay Kit and COD-PAP Cholesterol Assay Kit were provided by Nanjing Jiancheng Bioengineering Institute (Nanjing, China). Total RNA was extracted using the HiPure Total RNA Mini Kit from Guangzhou Magen Biotechnology Co., Ltd (Guangzhou, China). Reverse transcription was performed with HiScript® II Q RT SuperMix for qPCR (+gDNA wiper), and quantitative PCR was carried out using 2× RealStar Green Fast Mixture (Vazyme Biotech Co., Ltd, Nanjing, China). The Cell Counting Kit-8 (CCK-8) was obtained from Dojindo Molecular Technologies (Kumamoto, Japan). Antibodies against CD86 (polyclonal, Cat# bs-1035R) and CD206 (monoclonal, Cat# bsm-

60761R) were purchased from Biosynthesis Biotechnology Co., Ltd (Beijing, China).

2.2 Preparation of CHOL@CDNVs

2.2.1 Preparation of cholesterol-modified CDNVs. Cholesterol-modified CDNVs were prepared *via* the thin-film hydration method, adapted from a previously reported procedure.[31] Briefly, cholesterol was dissolved in a chloroform/ethanol mixture (2 : 1, v/v). The solvent was evaporated under reduced pressure (0.09 MPa) at 40 °C for 30 min using a rotary evaporator (RE-52AA, Shanghai Yarong) to form a dry lipid film. To incorporate cholesterol into the CDNVs membrane (for CDNVs preparation, see SI, Section 1.2), the dried film was hydrated within 1 mL of CDNVs suspension (1 mg mL^{-1} in PBS, pH 7.4). Cholesterol was add at three different masses: 10 μg, 50 μg, or 100 μg. The resulting formulations were designated as 1% CHOL@CDNVs, 5% CHOL@CDNVs, and 10% CHOL@CDNVs, corresponding to cholesterol-to-total CDNVs protein mass ratios of 1%, 5%, and 10%, respectively. Subsequently, the resulting suspension was sonicated on ice using a probe sonicator (JY92-IIN, Ningbo Scientz Biotechnology Co., Ltd, China; 6 mm probe diameter, 30 W power) with a cycle of 10 s pulse/10 s interval for a total duration of 5 min. The sonicated sample was then extruded 10 times through a 100 nm polycarbonate membrane (Millipore, USA) using an Avanti mini-extruder. Finally, the CHOL@CDNVs suspension was sterilized by filtration through a 0.22 μm pore-size membrane and stored at 4 °C in light-protected vials.

2.2.2 Preparation of fluorescein-DHPE-labeled vesicles. Fluorescent labeling of CDNVs and CHOL@CDNVs was performed using the thin-film hydration method. Briefly, fluorescein-DHPE (dissolved in dimethyl sulfoxide at 1 mg mL^{-1}) was mixed with the vesicle suspension at a mass ratio of 0.5% (w/w, relative to total lipid) under light-protected conditions. A lipid film was then formed, hydrated and extruded following the same procedure detailed in Section 2.2.1 to remove unincorporated fluorophores, the mixture was subjected to centrifugal filtration at 5000×*g* for 10 min at 4 °C using a 100 kDa molecular-weight-cutoff ultrafiltration device (Millipore, USA). The retained fraction containing the labeled vesicles was collected and stored in dark at 4 °C for subsequent cellular uptake studies.

2.3 Characterization of CHOL@CDNVs

2.3.1 Yield and physicochemical properties. The particle size distribution and concentration of CDNVs were determined using nanoparticle tracking analysis (NTA) on a NanoSight NS300 system (Malvern Instruments, UK). Total protein content was quantified with a bicinchoninic acid (BCA) protein assay kit (Nanjing Jiancheng Bioengineering Institute, China). The hydrodynamic diameter, polydispersity index (PDI) and zeta potential of CDNVs and CHOL@CDNVs were measured by dynamic light scattering (DLS) and electrophoretic light scattering using a Zetasizer Nano ZS90 system (Malvern Panalytical, UK).

2.3.2 Transmission electron microscopy. A 10 μL aliquot of CDNVs and CHOL@CDNVs suspension was deposited to a 230-mesh carbon-coated copper grid (Zhongjingkeyi Technology Co., Ltd, Beijing, China) and allowed to adsorb for 5 min. Excess liquid was carefully removed with filter paper. The grid was then negatively stained with 2% (w/v) phosphotungstic acid (pH 6.8) for 2 min and air-dried at room temperature. Morphological examination was performed using a JEM-1400Flash transmission electron microscope (JEOL Ltd, Japan) operated at an acceleration voltage of 120 kV.

2.4 Determination of cholesterol content in CHOL@CDNVs

The cholesterol content in 1% CHOL@CDNVs, 5% CHOL@CDNVs, and 10% CHOL@CDNVs was determined using a Total Cholesterol Assay Kit (Cat# A111-1-1, Nanjing Jiancheng Bioengineering Institute, China) according to the manufacturer's instructions. Absorbance was measured at 500 nm, and cholesterol concentrations were determined based on a standard calibration curve.

2.5 Stability evaluation of CHOL@CDNVs

The stability was assessed by storing the suspension (1 mg mL^{-1} in PBS, pH 7.4) at 4 °C under light-protected conditions. Changes in particle size, polydispersity index (PDI), and zeta potential were monitored on days 0, 7, 14, 21, and 28 using dynamic light scattering (Zetasizer Nano ZS90).

2.6 DPPH radical scavenging assay

A 0.2 mmol per L DPPH working solution was prepared by dissolving DPPH powder in anhydrous ethanol and stored in the dark at 4 °C. The test specimens included CDNVs isolated using 2.5%, 5%, or 10% PEG, as well as the formulations 1% CHOL@CDNVs, 5% CHOL@CDNVs, and 10% CHOL@CDNVs. All samples were adjusted to a particle concentration of approximately 5×10^{10} particles per mL in PBS. Equal volumes (100 μL each) of the DPPH working solution and sample solutions were combined in 1.5 mL microcentrifuge tubes, vortex-mixed for 10 s, and incubated at 25 °C in the dark for 30 min. After incubation, 200 μL of each reaction mixture was transferred to a 96-well plate. Absorbance was measured at 517 nm using a microplate reader, with anhydrous ethanol serving as the blank control. The radical scavenging rate was calculated according to the following formula:

$$\text{Scavenging rate}(\%) = \left[1 - \frac{A_s - A_0}{A_c}\right] \times 100\% \qquad (2\text{-}1)$$

where: A_c: absorbance of the DPPH solution control (without sample), A_0: absorbance of the anhydrous ethanol blank, A_s: absorbance of the sample after reaction with DPPH solution.

2.7 Cytotoxicity evaluation of CHOL@CDNVs

Cytotoxicity was evaluated using the Cell Counting Kit-8 (CCK-8) assay. RAW264.7 cells were seeded in 96-well plates and treated with CDNVs modified with 1%, 5%, or 10% cholesterol (*i.e.*, 1% CHOL@CDNVs, 5% CHOL@CDNVs, 10% CHOL@CDNVs) at

particle concentrations ranging from 0.03125 to 1×10^{10} particles per mL (0.03125, 0.0625, 0.125, 0.25, 0.5, and 1×10^{10} particles per mL) for 24 h. After treatment, 10 μL of CCK-8 reagent (Dojindo Molecular Technologies, Japan) was added to each well, followed by incubation at 37 °C for 2 h. Absorbance was measured at 450 nm using a microplate reader. Cell viability, was calculated as a percentage relative to untreated control cells using the following formula:

$$\text{Viability}\% = \frac{OD_{sample} - OD_{base}}{OD_{control} - OD_{base}} \times 100\% \quad (2\text{-}2)$$

where OD_{sample}, $OD_{control}$, OD_{base} represent the absorbances values of the treated cells, untreated control cells, and culture medium without cells, respectively.

2.8 Cellular uptake and endocytic mechanism of CHOL@CDNVs

2.8.1 Flow cytometry analysis of uptake. RAW264.7 macrophages were seeded in 6-well plates at a density of 1×10^6 cells per well and cultured overnight. Cells were then incubated with Fluorescein-DHPE-labeled CDNVs, 1% CHOL@CDNVs, 5% CHOL@CDNVs, or 10% CHOL@CDNVs at a final concentration of 0.5×10^{10} particles per mL for 24 h. After incubation, cells were washed three times with ice-cold PBS, harvested and immediately analyzed using a BD FACSCanto II flow cytometer (BD Biosciences, USA). Mean fluorescence intensity (MFI) was calculated with FlowJo v10 software (v1.53, National Institutes of Health, USA) to quantify vesicle uptake.

2.8.2 Confocal microscopy. For confocal imaging, RAW264.7 cells were seeded in confocal dishes at 1×10^4 cells per well and allowed to adhere overnight. Cells were treated with 1% CHOL@CDNVs, 5% CHOL@CDNVs, 10% CHOL@CDNVs, or unmodified CDNVs (0.5×10^{10} particles per mL) for 4 h, followed by three times PBS washes. Nuclei were stained with DAPI, and cellular internalization was visualized using a Zeiss LSM 800 confocal laser scanning microscope (Carl Zeiss, Germany). The fluorescence intensity of fluorescein-DHPE per cell was quantified with Image J software (v1.53, National Institutes of Health, USA).

2.8.3 Inhibition of endocytic pathways. To investigate the endocytic mechanisms, the concentrations of inhibitors were first optimized using CCK-8 assay to ensure non-cytotoxic conditions: Chlorpromazine (10 μM, clathrin-mediated endocytosis inhibitor), Wortmannin (50 μM, micropinocytosis inhibitor), and Filipin III (2.5 μM, caveolae-dependent endocytosis inhibitor). RAW264.7 cells were seeded in 96-well plates at 1×10^5 cells per well overnight. Following 1 h pretreatment with the respective inhibitors, cells were incubated with 1% CHOL@CDNVs, 5% CHOL@CDNVs, 10% CHOL@CDNVs, or unmodified CDNVs (0.5×10^{10} particles per mL) for 4 h. Cells were then washed and fluorescence intensity was measured using a Thermo Fisher microplate reader.

2.9 *In vitro* anti-inflammatory evaluation of CHOL@CDNVs

RAW264.7 macrophages were seeded in 6-well plates at a density of 1×10^6 cells per well and stimulated with 100 ng per mL LPS for 12 h to induce M1 polarization. Cells were then treated with CDNVs and 1%, 5%, or 10% CHOL@CDNVs at low (0.1×10^{10} particles per mL) and high (0.5×10^{10} particles per mL) concentrations for 24 h. Total RNA was extracted using the HiPure Total RNA Mini Kit according the manufacturer's protocol. cDNA was synthesized from 1 μg of total RNA using HiScript® II Q RT SuperMix. Real-time quantitative PCR (RT-qPCR) was performed using 2× RealStar Green Fast Mixture with GAPDH served as the endogenous reference gene for normalization. The relative expression levels of target genes (*TNF-α*, *IL-1β*, *iNOS*, *Arg-1*) were calculated using the $2^{-\Delta\Delta Ct}$ method. Primer sequences (see Table S1) were designed and synthesized by Shanghai Bioengineering Co., Ltd (China).

2.10 Flow cytometric analysis of macrophage phenotypes

RAW264.7 cells were seeded in 6-well plates at 1×10^6 cells per well and cultured overnight at 37 °C under 5% CO_2. To induce polarization, cells were stimulated for 12 h with either M1-polarizing inducers (100 ng per mL LPS) or M2-polarizing inducers (20 ng per mL IL-4 plus 20 ng per mL IL-13). Untreated cells served as M0-type control population. Polarized macrophages were subsequently incubated with CDNVs and 1%, 5%, or 10% CHOL@CDNVs at a final concentration of 0.5×10^{10} particles per mL for 24 h. Cells were then harvested and stained in the dark for 30 min with fluorochrome-conjugated antibodies: FITC- anti-mouse CD86 (for M1 identification) or APC- anti-mouse CD206 (MMR, for M2 identification) (BioLegend, USA). Following PBS wash, surface marker expression was analyzed on a BD FACSCanto II flow cytometer (BD Biosciences, USA). Data were processed using FlowJo v10 software to determine the percentages of $CD86^+$ (M1 phenotype) and $CD206^+$ (M2 phenotype) cell populations.

2.11 ROS scavenging evaluation of CHOL@CDNVs

RAW264.7 macrophages were seeded in 6-well plates at a density of 1×10^6 cells per well and stimulated with 100 ng per mL LPS for 12 h to induce M1 polarization. The cells were then treated with CDNVs and 1%, 5%, or 10% CHOL@CDNVs at a final concentration of 0.5×10^{10} particles per mL for 24 h. After three washes with PBS, cells were incubated with 10 μmol per L 2′,7′-dichlorodihydrofluorescein diacetate (DCFH-DA) at 37 °C for 20 min according to the manufacturer's instructions. Following additional PBS washes, intracellular ROS levels were immediately visualized using a Zeiss-800 confocal laser scanning microscope (CLSM, Germany). The fluorescence intensity of intracellular dichlorofluorescein (DCF) was quantified at the single-cell level using ImageJ software (v1.53, National Institutes of Health, USA).

2.12 *In vivo* therapeutic evaluation for ALI

2.12.1 LPS-induced ALI mouse model. Male BALB/c mice (7–8 weeks old, 17–22 g) were obtained from the Southern Medical University Animal Center and housed under standard conditions at Shaoguan University Animal Center. All experimental procedures were approved by the Institutional Animal Ethics Committee (Approval No.: 2024-DWLLSC-014) and

conducted in accordance with the 3R principles to minimize animal usage. After anesthesia induction, mice received intratracheal instillation of 50 μL sterile saline containing LPS (10 mg kg^{-1}) to establish the acute lung injury model. Mice in blank control group received an equal volume of PBS. Two hours post-instillation, mice were randomly divided into six groups ($n = 6$ per group) and treated *via* a medical nebulizer (Yuwell 403D, China) with 5 mL of the following: PBS (control), CDNVs, and 1%, 5%, or 10% CHOL@CDNVs (all at 1×10^{10} particles per mL). Mice were euthanized 24 h after treatment, and lung tissue along with serum samples were collected for subsequent analysis.

2.12.2 Lung wet/dry weight ratio. Freshly harvested lung tissues were immediately weighed to obtain the wet weight, then dried at 80 °C for 48 h until a constant dry weight was achieved. The extent of pulmonary edema was evaluated by calculating the lung wet/dry (W/D) weight ratio.

2.12.3 Histopathological analysis. Lung tissues were fixed in 4% paraformaldehyde, embedded in paraffin, and sectioned at 5 μm thickness for hematoxylin–eosin (H&E) and Masson's trichrome staining. Stained sections were digitally scanned using a NanoZoomer S360 system (Hamamatsu Photonics, Japan). Lung injury was evaluated using a modified Gao's scoring system.[33] Ten random fields per section (10× objective) was assessed for five histopathological parameters—(1) intra-alveolar neutrophils, (2) interstitial neutrophils, (3) hyaline membranes, (4) proteinaceous debris, and (5) alveolar septal thickening. Each parameter was scored from 0 to 2 based on severity and weighted scores were normalized per field to yield a final scores on a continuous scale from 0 to 1. For fibrosis assessment, collagen fibers stained blue in Masson's trichrome sections were measured within regions of interest using ImageJ s. Collagen deposition was semi-quantitatively scored as: 0 (none), 1 (mild, <25% field area), 2 (moderate, 25–50%), or 3 (severe, >50%).

2.12.4 Immunohistochemical (IHC) analysis. Tissue sections were incubated with primary antibodies against CD86 and CD206 at 4 °C overnight. After three washes with PBS, sections were treated with biotin-conjugated secondary antibodies in blocking buffer for 1 h at room temperature. Antigen-antibody complexes were visualized using 3,3′-diaminobenzidine (DAB) chromogen (Beyotime, China). All stained sections were scanned using a NanoZoomer S360 whole-slide scanner (Hamamatsu Photonics, Japan). The percentage area of CD86- and CD206-positive staining per field was quantified using ImageJ software, and the statistical comparisons of the positive staining area were performed between experimental groups.

2.12.5 Real-time quantitative PCR. Total RNA was extracted and purified from lung tissues using the HiPure Total RNA Mini Kit (Magen, China) according to the manufacturer's instructions. The relative expression levels of target genes were calculated using the $2^{-\Delta\Delta Ct}$ method and normalized to the control group.

2.12.6 Serum biochemical evaluation. Serum aspartate aminotransferase (AST) and alanine aminotransferase (ALT) activities were measured using commercial assay kits (Beyotime Biotechnology, China) strictly following the manufacturer's protocols. Enzyme activities are expressed in unit per liter (U L^{-1}).

2.13 Statistical analysis

All data were analyzed using GraphPad Prism software and are presented as mean ± standard deviation (SD) from at least three independent experiments. Statistical significance was determined by one-way or two-way analysis of variance (ANOVA) with appropriate *post hoc* tests. Significance levels were defined as follows: ns, not significant, $*P < 0.05$, $**P < 0.01$, $***P < 0.001$.

3 Results and discussion

3.1 Preparation and characterization of cholesterol-modified CDNVs (CHOL@CDNVs)

CDNVs were successfully isolated from *Clematis filamentosa* Dunn leaves using three methods: ultrafiltration, sucrose-density-gradient ultracentrifugation, and polyethylene glycol (PEG) precipitation[34] (Fig. S1A). Nanoparticle tracking analysis (NTA) revealed that the particle numbers of CDNVs obtained by PEG precipitation, ultracentrifugation, and ultrafiltration were $(69.01 \pm 1.22) \times 10^{11}$ particles per mL, $(7.84 \pm 0.99) \times 10^{11}$ particles per mL, and $(2.26 \pm 0.82) \times 10^{11}$ particles per mL, respectively (Fig. S1B and C). The purity of each preparation was assessed by the ratio of particle numbers to total protein content, which indicated the order: CDNVs2 > CDNVs3 > CDNVs1 (Fig. S1D). Although sucrose-density-gradient ultracentrifugation is widely regarded as the gold-standard method for obtaining high-purity vesicles, its comparatively low yield may be attributed to unavoidable vesicle loss during the centrifugation.[35] Therefore, PEG precipitation was selected for further optimization. We systematically evaluated different concentrations of PEG8000 (2.5%, 5%, and 10%), with the resulting vesicle formulations designated as 2.5% CDNVs, 5% CDNVs, and 10% CDNVs, respectively (Fig. 1A). Yield analysis showed corresponding particle numbers of $(67.63 \pm 1.56) \times 10^{11}$ particles per mL, $(69.01 \pm 1.22) \times 10^{11}$ particles per mL, and $(80.11 \pm 2.29) \times 10^{11}$ particles per mL for the 2.5%, 5%, and 10% groups, respectively. The particle-to-total protein ratio indicated that 5% CDNVs exhibited the highest purity (Fig. 1C). Consequently, 5% PEG8000 was established as the optimal condition for standard extraction.

The mean particle diameters, as determined by dynamic light scattering (DLS) were 115.55 ± 4.32 nm (2.5% CDNVs), 110.77 ± 4.75 nm (5% CDNVs), and 95.19 ± 5.08 nm (10% CDNVs), with corresponding polydispersity indices (PDI) all below 0.2, indicating a monodisperse distributions (Fig. 1D). The decrease in particle size with increasing PEG concentration is consistent with the selective precipitation of smaller vesicles promoted by higher polymer concentrations.[36] Transmission electron microscopy (TEM) further confirmed the presence of spherical, bilayer-membrane nanostructures, which is typical of plant-derived extracellular vesicles. Zeta potential analysis revealed moderately negative surface charges of −11.10 ± 1.33 mV (2.5% CDNVs), −10.50 ± 1.75 mV (5% CDNVs), and

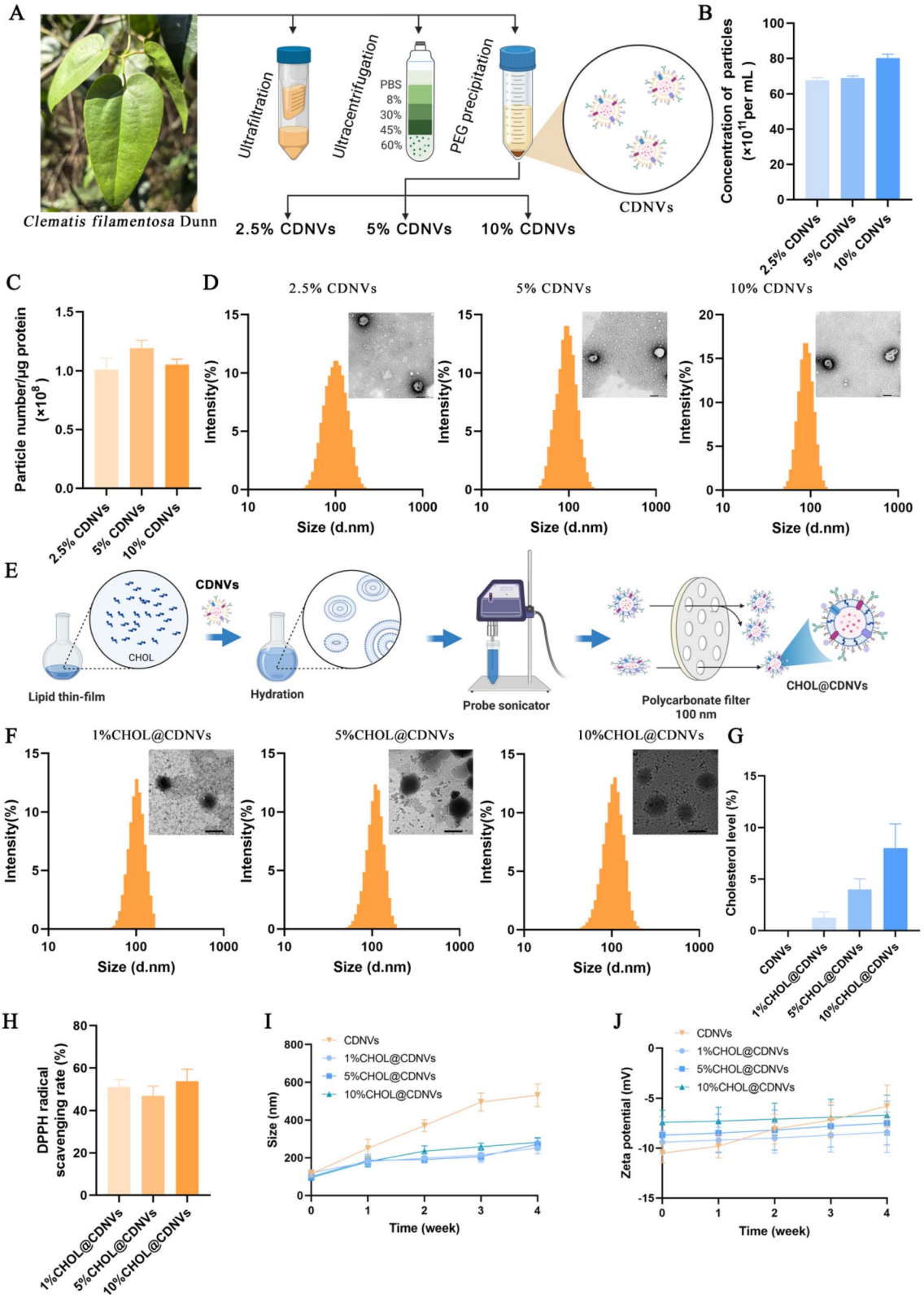

Fig. 1 Preparation and characterization of CHOL@CDNVs. (A) Schematic illustration of nanovesicles isolation from *Clematis filamentosa* Dunn leaves. (B) Particle number of CDNVs obtained at different PEG concentrations, as determined by nanoparticle tracking analysis (NTA). (C) Purity, expressed as the particle to protein ratio (particle number per μg protein). (D) Particle size distribution (DLS) and representative TEM images of CDNVs isolated with 2.5%, 5%, and 10% PEG. Scale bar = 100 nm. (E) Schematic illustration of the fabrication process of CHOL@CDNVs. (F) Size distribution (DLS) and corresponding TEM images of 1%, 5%, and 10% CHOL@CDNVs. Scale bar = 100 nm. (G) Cholesterol incorporation efficiency in CHOL@CDNVs. (H) Antioxidant capacity evaluated by DPPH radical scavenging assay. (I) Particle size stability assessment. (J) Zeta potential stability assessment.

−9.85 ± 2.08 mV (10% CDNVs), a profile likely due to the presence of exposed acidic phospholipids on the vesicle surface.

The antioxidant capacity of the vesicles was assessed by DPPH radical scavenging assays at a concentration of approximately 5×10^{10} particles per mL. The scavenging rates were 35.8 ± 2.78%, 44.1 ± 2.69%, and 38.4 ± 4.23% for 2.5% CDNVs, 5% CDNVs, and 10% CDNVs, respectively. For comparison, CDNVs isolated by ultrafiltration (CDNVs1) and ultracentrifugation (CDNVs2) showed scavenging activities of 24.1 ± 3.22% and 50.2 ± 4.26%, respectively (Fig. S1E). These results suggest that the DPPH radical scavenging activity of CDNVs correlates with preparation purity, wherein higher-purity vesicles exhibit enhanced antioxidant effects. Furthermore, these findings support the potential of CDNVs as a reliable platform for antioxidant therapies.

Lipidomic analysis revealed that the CDNVs membranes was enriched in diacylglycerol (DG, 16%) and monogalactosyldiacylglycerol (MGDG, 10%). Phosphatidylinositol (PI), phosphatidylcholine (PC), digalactosyldiacylglycerol (DGDG), and phosphatidylethanolamine (PE) were also detected, each constituting approximately 8% of the lipid profile (Fig. S2). DG has been reported to alleviate hyperuricemia-induced renal inflammation and systemic oxidative stress by suppressing xanthine oxidase (a key mediator of oxidative stress) and modulating gut microbiota dysbiosis, thereby exhibiting dual anti-inflammatory and antioxidant properties.[37] Moreover, DG can enhance the performance of nanovesicle by improving colloidal stability and the bioavailability of encapsulated bioactive compounds.[38] MGDG, PC, and PE are also known to participate in redox homeostasis and anti-inflammatory responses through mechanisms such as TLR4/MD-2 complex antagonism, PI3K/AKT/MAPK pathway regulation, and membrane fluidity stabilization.[39–41] Notably, cholesterol was not detected in native CDNVs. This absence of endogenous cholesterol thereby provides an opportunity for tailored membrane engineering *via* exogenous cholesterol modification to enhance vesicle stability.

To engineer the vesicle membrane, cholesterol was incorporated into CDNVs membrane at low, medium, and high concentrations using a thin-film hydration method followed by sonication and extrusion. The resulting formulations were designated as 1% CHOL@CDNVs, 5% CHOL@CDNVs, and 10% CHOL@CDNVs, corresponding to cholesterol-to-total protein mass ratios of 1%, 5%, and 10%, respectively (Fig. 1E). DLS measurements indicated a cholesterol-dependent increase in the mean particle sizes: 91.18 ± 4.55 nm for 1% CHOL@CDNVs, 98.74 ± 4.78 nm for 5% CHOL@CDNVs, and 118.28 ± 5.05 nm for 10% CHOL@CDNVs. All formulations maintained a low PDI (<0.2), indicating homogeneous dispersion. TEM confirmed that the spherical morphology and uniform size distribution (approximately 100 nm) of CDNVs were well preserved after cholesterol modification, with no observable morphological alterations compared to the unmodified CDNVs (Fig. 1F). Zeta potential measurements showed surface charges of −9.4 ± 1.21 mV, −8.7 ± 1.86 mV, and −7.4 ± 1.15 mV for the three groups. The gradual decrease in surface negativity with higher cholesterol content is likely due to cholesterol insertion altering membrane architecture and partially shielding the negatively charged groups of acidic phospholipids.

Cholesterol oxidase-based quantification confirmed a very low intrinsic cholesterol level of 0.038 ± 0.007% in unmodified CDNVs. The actual incorporation efficiencies for the three modified groups were quantified as 1.26 ± 0.56%, 4.01 ± 1.02%, and 8.02 ± 2.35% for the 1%, 5%, and 10% theoretical cholesterol incorporation groups, respectively (Fig. 1G). These results collectively confirm the successful incorporation of cholesterol onto the CDNVs membrane. Furthermore, the strong positive correlation observed between the actual incorporation efficiency and the intended cholesterol concentration validates the efficiency and controllability of our preparation method. The DPPH radical scavenging capacity of the three CHOL@CDNVs formulations (at 5×10^{10} particles per mL) was 51.04 ± 2.11% (1% CHOL@CDNVs), 46.94 ± 1.87% (5% CHOL@CDNVs), and 53.82 ± 2.35% (10% CHOL@CDNVs). No statistically significant differences were observed among the groups ($P > 0.05$), suggesting that cholesterol modification did not significantly alter the intrinsic antioxidant activity of CDNVs (Fig. 1H).

After storage at 4 °C for 4 weeks, the CHOL@CDNVs formulations showed no signs of visible aggregation (Fig. S3). Dynamic monitoring of particle size revealed that the 1–10% CHOL@CDNVs formulations exhibited only a 133–163% (initial: 95–120 nm *vs.* post-storage: 250–280 nm) increase after storage, demonstrating a markedly low degree of aggregation compared to the 360% increase observed in unmodified CDNVs (Fig. 1I). All cholesterol-modified CDNVs maintained a stable PDI, fluctuating below 0.15 (initial: 0.10 ± 0.02 *vs.* post-storage: <0.25), thereby meeting the accepted stability criteria for nanoformulations. Following storage, CHOL@CDNVs exhibited superior surface-charge stability compared to unmodified CDNVs. The zeta potential change ($\Delta\zeta$) for unmodified CDNVs was 4.72 mV, whereas for all CHOL@CDNVs formulations the variations was limited to a narrow range of 0.7–1.2 mV (Fig. 1J). Collectively, these results demonstrate that cholesterol modification significantly enhances the structural stability of CDNVs during short-term storage at 4 °C. This stabilizing effect is consistent with the known role of cholesterol in increasing lipid bilayers rigidity, thereby suppressing vesicle fusion and rupture.[41]

3.2 Cellular uptake efficiency and mechanisms of CHOL@CDNVs

Prior to investigating the interaction between CHOL@CDNVs and RAW264.7 macrophages, we first evaluated their cytocompatibility using the CCK-8 assay. RAW264.7 cells were treated for 24 hours with CDNVs, 1% CHOL@CDNVs, 5% CHOL@CDNVs, or 10% CHOL@CDNVs at concentrations ranging from 0 to 100 μg mL^{-1}. The CCK8 assay showed that cell viability was maintained above 80% in all treatment groups at concentration up to 100 μg mL^{-1} (Fig. 2A), demonstrating the absence of significant cytotoxicity of CHOL@CDNVs at the tested concentrations.

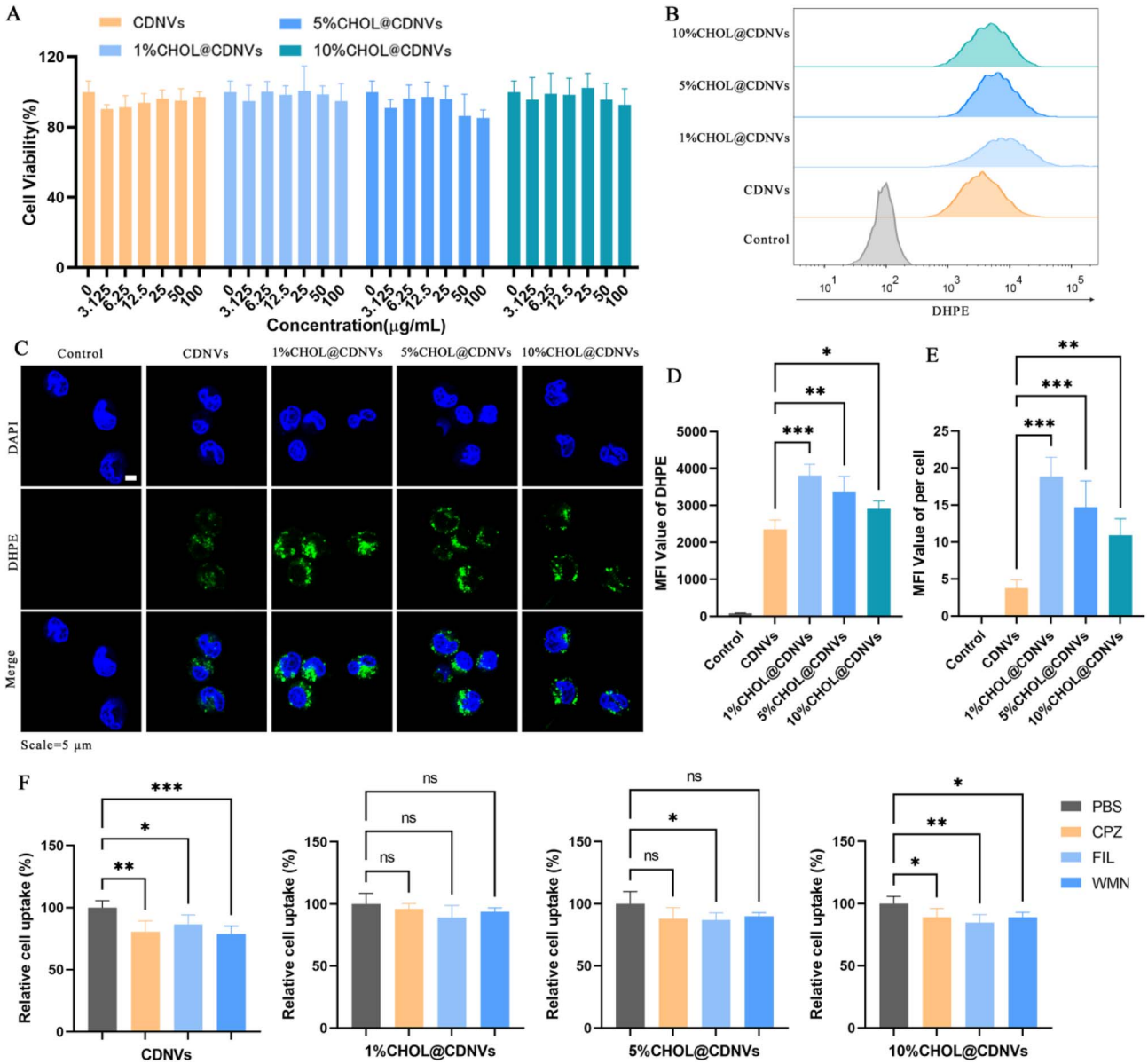

Fig. 2 Cellular uptake efficiency and mechanisms of CHOL@CDNVs. (A) Cytocompatibility of CHOL@CDNVs in RAW264.7 macrophages assessed by CCK8 assay. (B) Quantitative analysis of cellular uptake by flow cytometry. (C) Fluorescence microscopy images visualizing localization of CHOL@CDNVs. Scale bar = 5 μm. (D) Quantification of cellular uptake levels. (E) Mean fluorescence intensity (MFI) per cell from image analysis. (F) Effects of endocytic inhibitors on cellular uptake: chlorpromazine (CPZ, clathrin-mediated), filipin III (FIL, caveolae-dependent), and wortmannin (WMN, macropinocytosis). Data are presented as mean ± SD, *$P < 0.05$, **$P < 0.01$, ***$P < 0.001$.

To assess the cellular uptake capacity, RAW264.7 cells were incubated with DHPE-labeled CDNVs and CHOL@CDNVs variants. Flow cytometric analysis revealed that the mean fluorescence intensity (MFI) was significantly enhanced in the cholesterol-modified groups, showing 1.6-fold, 1.4-fold, and 1.2-fold increase for the 1%, 5%, and 10% CHOL@CDNVs, respectively, compared to unmodified CDNVs (Fig. 2B and D), indicating that cholesterol modification significantly promotes macrophage uptake. Consistent with the flow cytometry result, fluorescence microscopy after 4 hours of co-incubation confirmed that both CDNVs and CHOL@CDNVs were effectively internalized by RAW264.7 cells (Fig. 2C). Quantification of MFI per cell confirmed a significant enhancement in uptake, with the 1%, 5%, and 10% CHOL@CDNVs groups exhibited 5.1-fold, 3.9-fold, and 2.9-fold higher intensities, respectively, compared to the unmodified CDNVs group (Fig. 2E). Together, these data demonstrate that cholesterol modification significantly enhances cellular uptake of CDNVs. Notably, the 1% CHOL@CDNVs formulation exhibited the highest uptake efficiency, indicating an inverse relation between the cholesterol modification and uptake enhancement.

The cellular uptake mechanisms of CHOL@CDNVs were investigated using specific endocytic pathway inhibitors at concentrations pre-validated for cell safety (determined by CCK-8 assay, Fig. S3): 10 μM chlorpromazine (CPZ) for clathrin-mediated endocytosis, 2.5 μM filipin III (FIL) for caveolae-

dependent endocytosis and 50 μM wortmannin (WMN) for macropinocytosis. Following inhibitor pretreatment, the cellular uptake of CDNVs was significantly reduced by 19.5% with CPZ, 14.5% with FIL, and 22.3% with WMN (Fig. 2F), suggesting the involvement of clathrin-mediated endocytosis, caveolae-mediated endocytosis, and micropinocytosis in the internalization process. Notably, cholesterol modification significantly attenuated the inhibitor-induced reduction in cellular uptake in a cholesterol concentration-dependent manner. For 1% CHOL@CDNVs, cellular uptake was marginally reduced by 3.9% (CPZ), 10.9% (FIL), and 6.2% (WMN) following inhibitor pretreatment ($P > 0.05$). The attenuated inhibitory effects suggest a potential shift toward an energy-independent membrane fusion mechanism, rather than reliance on canonical clathrin- or caveolae-mediated endocytic pathways. Conventional cholesterol-containing carriers typically utilize direct membrane fusion as an energy-favorable alternative to receptor-dependent endocytosis.[42] Contrary to the established role of cholesterol in promoting membrane fusion in synthetic lipid carriers, our data reveal that a low modification ratio (1%), rather than high cholesterol content, significantly enhances this uptake process in CDNVs.[43,44] Collectively, these findings establish a novel design principle for plant-derived nanovesicles, wherein strategic low-dose cholesterol modification enhances energy-conserving cellular uptake mechanisms, thereby achieving substantial improvement in drug delivery efficacy.

3.3 CHOL@CDNVs modulate macrophage polarization and antioxidant activity

Dysregulated macrophage activation serves as key driver of ALI progression, primary through excessive generation of reactive oxygen species (ROS) and sustained release of pro-inflammatory cytokine.[45] To investigate the regulatory effects of CHOL@CDNVs on macrophage polarization and antioxidant activity, we established an *in vitro* cell model of LPS-stimulated RAW264.7 macrophages, which recapitulates the key pathological features of pro-inflammatory activation and oxidative stress.

The anti-inflammatory capacity of CDNVs and CHOL@CDNVs was first assessed by RT-qPCR, measuring the mRNA levels of LPS-induced pro-inflammatory cytokines (*TNF-α*, *IL-1β*) and macrophage polarization markers (*iNOS* for M1, *Arg-1* for M2). As expected, LPS stimulation significantly upregulated the mRNA expression of the pro-inflammatory *TNF-α* and *IL-1β*, concurrent with a marked increase in the *iNOS*/*Arg-1* ratio ($P < 0.05$), confirming a shift towards the pro-inflammatory M1 phenotype (Fig. 3A). At a concentration of 50 μg mL^{-1} (high concentration, H), both CDNVs and CHOL@CDNVs significantly suppressed the LPS-induced mRNA expression of *TNF-α* and *IL-1β* ($P < 0.05$). The 1% CHOL@CDNVs formulation showed the most potent effect, reducing *TNF-α* and *IL-1β* levels by 67.2% and 54.1%, respectively, compared to the PBS-treated controls ($P < 0.01$). Furthermore, cholesterol modification significantly lowered the *iNOS*/*Arg-1* ratio (40% reduction *vs.* CDNVs group, $P < 0.001$), indicating that its anti-inflammatory mechanism involves suppression of M1 polarization.

To further validate the polarization regulation, we performed flow cytometry analysis of M1 marker CD86 and M2 marker CD206. LPS stimulation drastically increased the proportion of $CD86^+$ cells from a baseline of 0.5% ± 0.1% to 96.7% ± 10.5% ($P < 0.001$). Treatment with either CDNVs or CHOL@CDNVs significantly attenuated this LPS-induced increase in $CD86^+$ populations (Fig. 3B). The 1% CHOL@CDNVs group exhibited the most substantial suppression of M1 polarization, showing the lowest $CD86^+$ percentage (31.5% ± 4.9%), which corresponded to a 65% reduction compared to the LPS group ($P < 0.001$). Furthermore, to assess M2-promoting activity, we employed an IL-4/IL-13-induced M2 model. In this setting, 1% CHOL@CDNVs induced a striking 27-fold increase in the $CD206^+$ cell proportion (41.6% ± 1.1%) over the M0 controls (1.5% ± 0.2%, $P < 0.001$), a level that was also significantly higher than that achieved by plain CDNVs (11.2% ± 0.8%, $P < 0.01$) (Fig. 3C).

Intracellular ROS levels were measured using the fluorescent probe DCFH-DA (2′,7′-dichlorodihydrofluorescein diacetate), which can be oxidized by ROS to form the highly fluorescent compound DCF. LPS stimulation triggered a sharp, 30.3-fold increase in DCF fluorescence intensity compared to the control controls ($P < 0.001$). In contrast, treatment with either CDNVs or CHOL@CDNVs produced a significant attenuation of LPS-induced ROS elevation (Fig. 3D). Semi-quantitative analysis revealed that ROS levels were reduced to 3.6% ± 1.5%, 18.1% ± 3.9%, and 30.7% ± 5.4% of the PBS control level in the 1%, 5%, and 10% CHOL@CDNVs groups, respectively ($P < 0.001$) (Fig. S4). Notably, the 1% CHOL@CDNVs exhibited a 1.5-fold greater ROS scavenging efficiency than CDNVs ($P < 0.01$), demonstrating that the low-level cholesterol modification synergistically augments the inherent antioxidant activity. These results suggest that enhanced macrophage uptake mediated by low-level cholesterol modification amplifies the intracellular antioxidant and anti-inflammatory effects of CHOL@CDNVs.

3.4 Therapeutic efficacy of CHOL@CDNVs in murine acute lung injury

To evaluate the *in vivo* therapeutic efficacy of CHOL@CDNVs, we employed a mouse model of acute lung injury (ALI) induced by lipopolysaccharide (LPS). In this model, LPS instigation leads to alveolar-capillary damage, primary driven by the activation of robust inflammatory cascades and oxidative stress.[46] Following 24-hour nebulized inhalation of PBS, CDNVs, or CHOL@CDNVs (1%, 5%, 10%), pulmonary histopathology and therapeutic outcomes were systematically evaluated (Fig. 4A). Macroscopic observation of LPS-challenged lungs showed diffuse congestion, edema, and consolidation, characterized by increased lobar volume, dark red hemorrhagic foci, and yellowish frothy exudates on the section planes (Fig. 4B). In contrast, the gross pathology was marked ameliorated in CHOL@CDNVs-treated groups, particularly at the 1% ratio, which displayed substantially reduced areas of congestion, edema, and hemorrhage, suggesting improved pulmonary microcirculation and diminished alveolar fluid leakage.

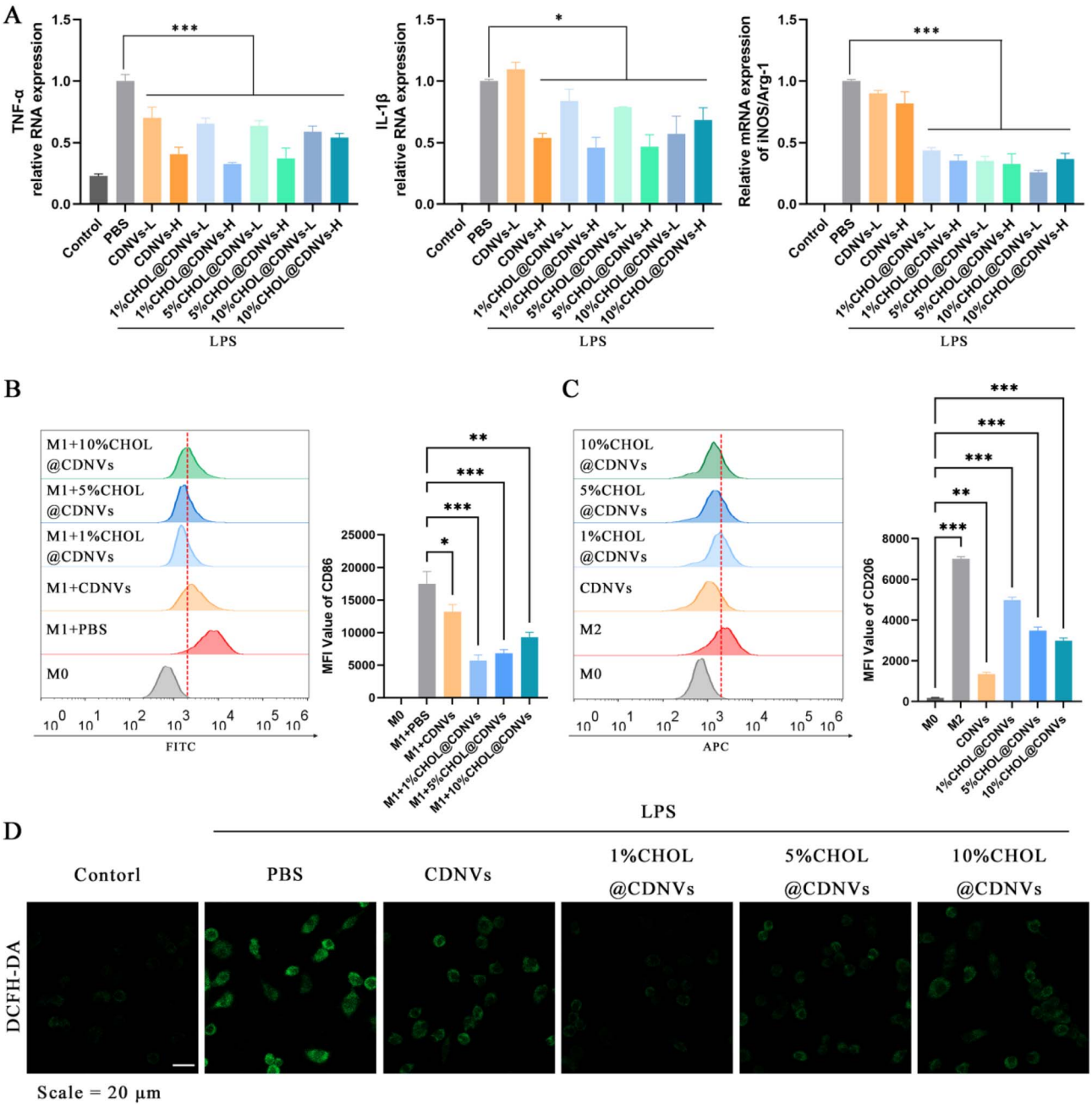

Fig. 3 Modulation of macrophage polarization and intracellular ROS by CHOL@CDNVs. (A) mRNA expression levels of pro-inflammatory cytokines (*TNF-α, IL-1β*) and the *iNOS/Arg-1* ratio (M1/M2 polarization markers), as determined by RT-qPCR. (B) Phenotypic analysis of M1 macrophages *via* CD86 staining and corresponding quantitative flow cytometry analysis. (C) Phenotypic analysis of M2 macrophages *via* CD206 staining and corresponding quantitative flow cytometry analysis. (D) Representative fluorescence images of intracellular ROS levels using DCFH-DA staining. Scale bar = 20 μm. Data are presented as mean ± SD, $^{*}P < 0.05$, $^{**}P < 0.01$, $^{***}P < 0.001$.

H&E staining revealed distinct histological profiles across groups. Lungs from normal control mice exhibited thin alveolar walls and intact architecture. In contrast, LPS-challenged lungs showed markedly thickened alveolar septa and dense inflammatory infiltration by neutrophils and macrophages. All vesicle-treated groups exhibited varying degrees of architectural restoration, with the 1% CHOL@CDNVs group showing the most pronounced reduction in both alveolar wall thickness and inflammatory cell infiltration compared to the LPS controls (Fig. 4C). Lung injury scores were quantified according to established histopathological criteria, including inflammatory cells infiltration, hemorrhage, and alveolar septal integrity. The LPS group exhibited a severe injury score of 0.80, whereas the 1% CHOL@CDNVs group showed the most substantial improvement, with the lowest score of 0.38. A clear trend of concentration-dependent efficacy was observed across the other groups: CDNVs (0.64), 10% CHOL@CDNVs (0.51), and 5% CHOL@CDNVs (0.50) (Fig. 4D).

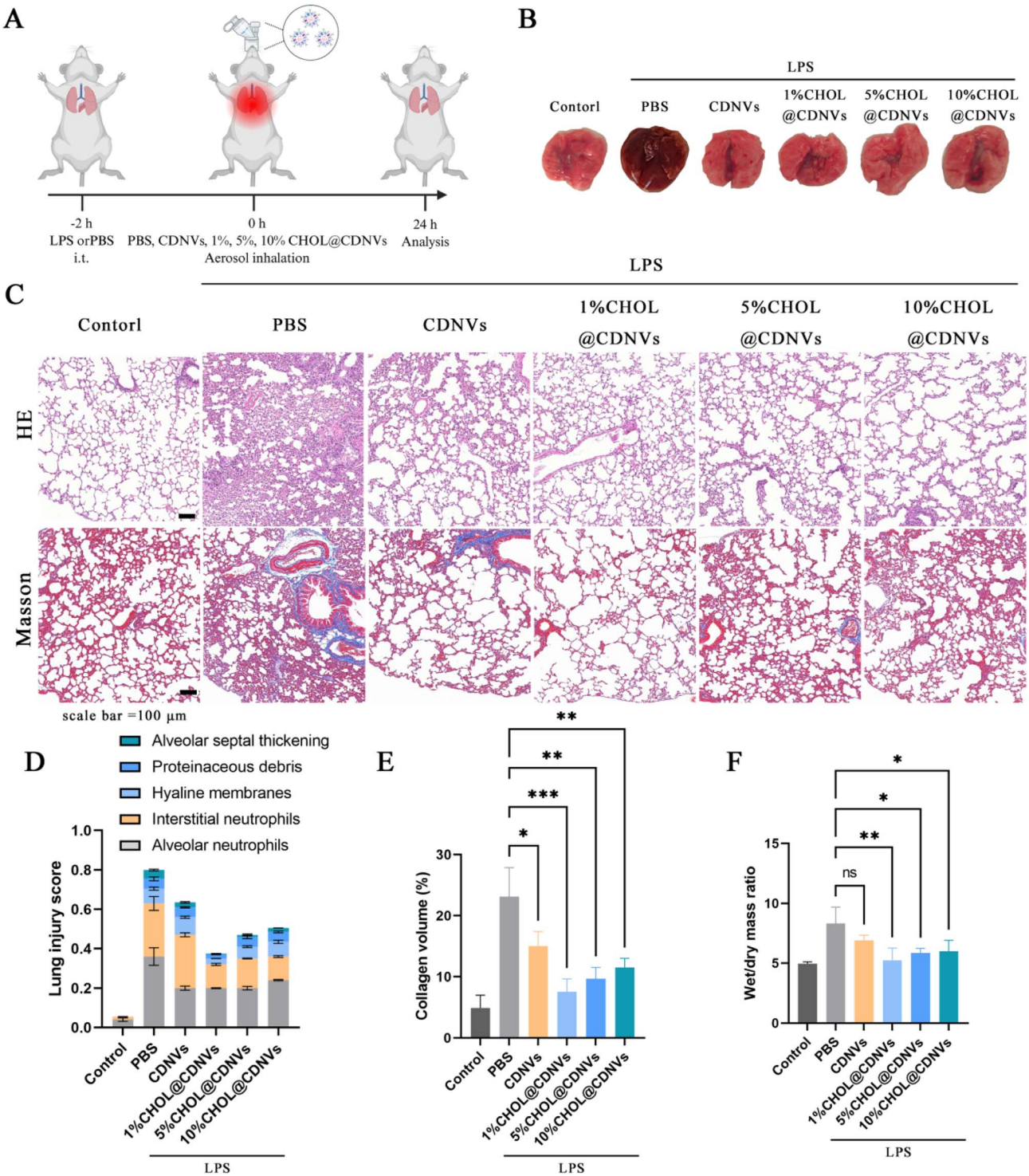

Fig. 4 Therapeutic efficacy of CHOL@CDNVs in a murine model of acute lung injury. (A) Schematic illustration of the experimental timeline and treatment protocol. (B) Representative gross morphological appearance of lung tissue from different treatment groups. (C) Histopathological analysis by H&E staining (upper panel) and Masson's trichrome staining (lower panel) for collagen deposition. Scale bar = 100 μm. (D) Semi-quantitative assessment of lung injury severity based on established histopathological criteria. (E) Quantitative analysis of pulmonary collagen content. (F) Evaluation of pulmonary edema using the lung wet/dry (W/D) weight ratio. Data are presented as mean ± SD, $*P < 0.05$, $**P < 0.01$, $***P < 0.001$.

Masson's trichrome staining demonstrated a 4.7-fold increase in collagen fiber deposition (blue-stained areas) within the pulmonary interstitium of the LPS group compared to normal controls ($P < 0.001$). This LPS-induced fibrosis was significantly attenuated in all CHOL@CDNVs treatment groups. Quantitative assessment confirmed that 1% CHOL@CDNVs

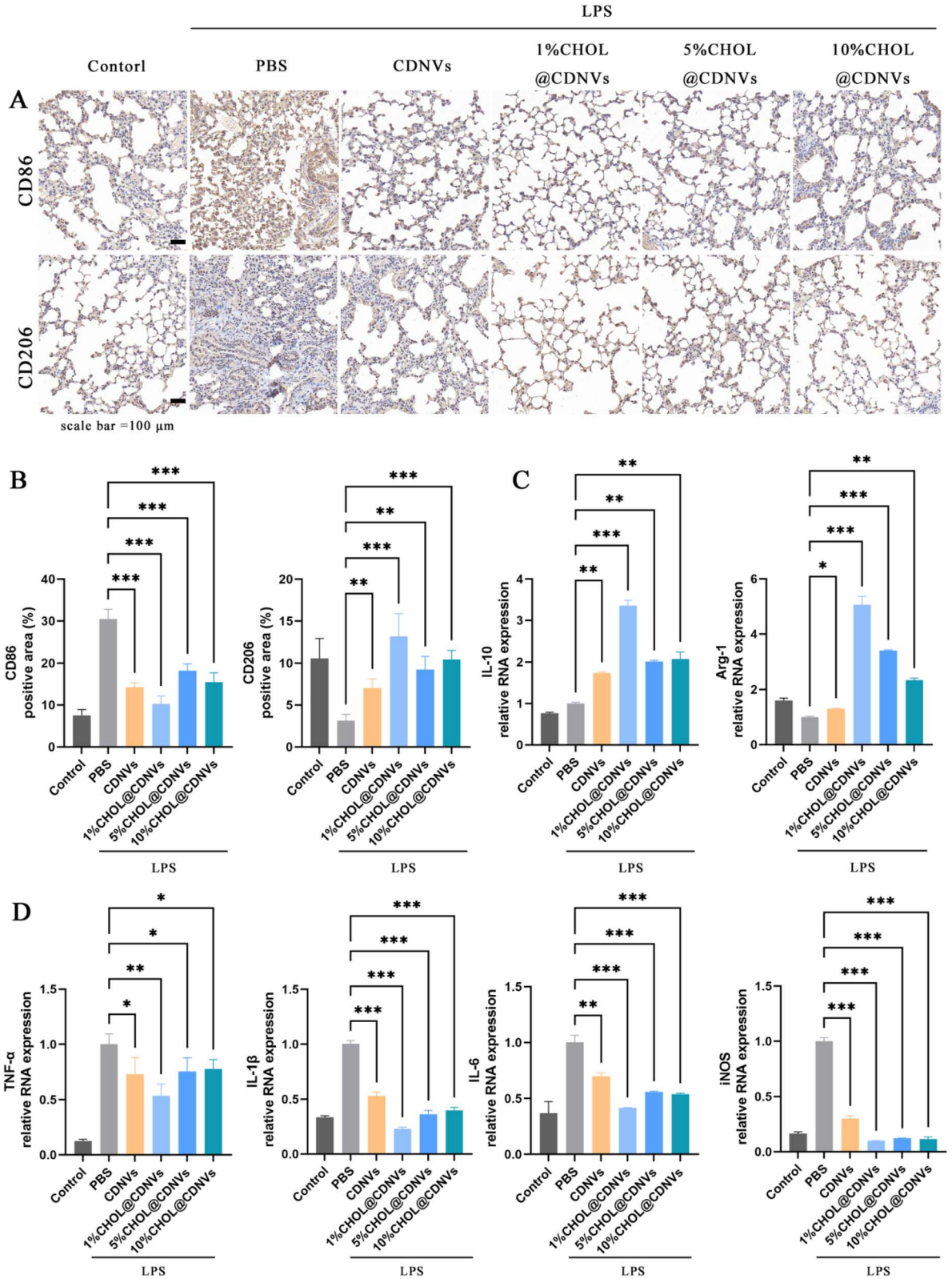

Fig. 5 CHOL@CDNVs modulate inflammatory responses in a murine model of acute lung injury. (A) Representative immunohistochemical (IHC) staining of M1 (CD86, upper panel) and M2 (CD206, lower panel) macrophage markers in lung tissue. Scale bar = 100 μm. (B) Quantification of $CD86^+$ and $CD206^+$ areas from IHC analysis. (C) mRNA expression levels of anti-inflammatory markers (*IL-10*, *Arg-1*) (D) mRNA expression profiles of pro-inflammatory mediator (*TNF-α*, *IL-1β*, *IL-6*, *iNOS*). Data are presented as mean ± SD, $^*P < 0.05$, $^{**}P < 0.01$, $^{***}P < 0.001$.

achieved a 67.3% ± 2.1% reduction in collagen area compared to the LPS group ($P < 0.001$), demonstrating superior efficacy over both the unmodified CDNVs (35.0% ± 2.4%) and the other cholesterol-modified formulations (Fig. 4E). The lung wet/dry (W/D) weight ratio, an indicator of pulmonary edema, was elevated by 68.2% elevation in the LPS group compared to normal controls. Treatment with 1% CHOL@CDNVs restored the W/D ratio to a level comparable to that of normal controls (5.2 ± 1.0 *vs.* normal 4.9 ± 0.2, $P > 0.05$), demonstrating superior efficacy to other treatment groups (Fig. 4F).

3.5 CHOL@CDNVs modulate pulmonary macrophage polarization and inflammation

To delineate the immunomodulatory mechanisms of CHOL@CDNVs in the lung microenvironment, we performed immunohistochemistry (IHC) and molecular analyses. IHC of lung sections (Fig. 5A) showed that LPS challenge markedly elevated $CD86^+$ expression while suppressing $CD206^+$, indicating a dominant M1-polarized macrophage response and aggravated inflammation. Nebulized delivery of CHOL@CDNVs substantially reversed this inflammatory polarization. The 1% CHOL@CDNVs group most effectively reversed the LPS-induced polarization imbalance, showing a 66.3% ± 1.9% reduction in $CD86^+$ expression ($P < 0.001$ *vs.* PBS) and a 3.1-fold increase in $CD206^+$ expression ($P < 0.001$). This dual immunomodulatory efficacy significantly surpassed that of unmodified CDNVs, which reduced CD86 by 53.2% ± 1.1% and elevated CD206 by only 1.2-fold ($P < 0.01$), demonstrating that low-concentration cholesterol modification confers and enhanced capacity to reprogram macrophage polarization (Fig. 5B).

RT-qPCR analysis (Fig. 5C and D) revealed that LPS challenge induced a dysregulated expression profile, characterized by significant upregulation of pro-inflammatory cytokines (*TNF-α*, *IL-1β*, *IL-6*) and the M1 marker *iNOS* ($P < 0.001$), coupled with downregulation of the anti-inflammatory cytokines *IL-10* and M2 marker *Arg-1* ($P < 0.01$) A 24-hour treatment with CHOL@CDNVs resulted in a coordinated attenuation and restoration, significantly reducing the expression of pro-inflammatory mediators ($P < 0.05$) while elevating the levels of *IL-10* and *Arg-1* levels ($P < 0.01$). It is noteworthy that the 1% CHOL@CDNVs group elicited the most pronounced immunomodulatory effect, achieving significantly greater suppression of pro-inflammatory factors and a strong elevation of anti-inflammatory mediators compared to both unmodified CDNVs and the higher-concentration CHOL@CDNVs groups ($P < 0.01$).

Biosafety evaluation confirmed that CHOL@CDNVs administration at therapeutic dose induced no significant systemic toxicity. Body weight progression was comparable across all groups throughout the study. Furthermore, key hepatic function markers, including ALT (38–40 U L^{-1}) and AST (55–60 U L^{-1}), were comparable between the CHOL@CDNVs-treated and control groups ($P > 0.05$, Fig. S5), confirming the excellent biocompatibility of the formulations. These findings collectively demonstrate that CHOL@CDNVs ameliorate acute lung injury (ALI/ARDS) progression through a multimodal mechanism involving the rebalancing of macrophage M1/M2 polarization, suppression of pro-inflammatory cytokine secretion, and promotion of an anti-inflammatory microenvironment. Together with its favorable *in vivo* safety profile, this nanoplatform showed translational promise as an integrated antioxidant and anti-inflammatory therapeutic platform.

4 Conclusion

This study successfully developed cholesterol-modified nanovesicles derived from *Clematis filamentosa* Dunn leaves (CHOL@CDNVs), which exhibited uniform particle size distribution and improved colloidal stability. Low-concentration cholesterol modification enhanced macrophage uptake efficiency by 1.6-fold and significantly improved the vesicles' ability to regulate M1 macrophage-mediated oxidative stress and inflammatory responses, while simultaneously promoting M2 macrophage polarization. In a murine model of LPS-induced acute lung injury, nebulized administration of 1% CHOL@CDNVs effectively reverse pulmonary pathophysiology, normalizing lung wet/dry weight ratios and markedly improving histophysiological outcomes through rebalancing macrophage polarization and suppression pro-inflammatory pathways. These findings propose an innovative strategy for functional engineering of plant-derived nanovesicles and establish an experimental basis for effective antioxidant and anti-inflammatory combination therapy in ALI/ARDS.

Author contributions

Guanglin Zhang, Huadong Liang: conceptualization, methodology, validation, formal analysis, investigation, data curation, writing – original draft. Guanyan Zhang, Changyao Chen, Junjie Lai, Hongjia Huang and Liubing Hu: validation, investigation. Baiyin Yu and Xiang Li: resources, project administration, funding acquisition. Rong Zeng and Chen Jie: methodology, supervision, writing – review & editing, funding acquisition. All authors read and contributed to the manuscript.

Conflicts of interest

The author(s) report no conflicts of interest in this work.

Abbreviations

ALI	Acute lung injury
ALT	Alanine aminotransferase
ARDS	Acute respiratory distress syndrome
AST	Aspartate aminotransferase
ATCC	American type culture collection
BCA	Bicinchoninic acid
CCK-8	Cell counting kit-8
CDNVs	*Clematis filamentosa* Dunn.-derived nanovesicles
CHOL	Cholesterol
CHOL@CDNVs	Cholesterol-modified CDNVs

CPZ	Chlorpromazine
DCF	Dichlorofluorescein
EVs	Extracellular vesicles
FIL	Filipin III
H&E	Hematoxylin–eosin
LPS	Lipopolysaccharide
IHC	Immunohistochemical
MEVs	Mammalian-derived EVs
NTA	Nanoparticle tracking analysis
PBS	Phosphate-buffered saline
PDI	Polydispersity index
PEG	Polyethylene glycol
PEVs	Plant-derived extracellular vesicle
ROS	Reactive oxygen species
RT-qPCR	Real-time quantitative PCR
WMN	Wortmannin

Data availability

The data that support the findings of this study are available from the corresponding authors upon reasonable request.

Supplementary information (SI): methods: RAW264.7 cell culture; CDNVs isolation; lipidomic profiling protocol; and RT-PCR primer sequences. Results: physicochemical characterization of CDNVs; lipidomic profiles; stability assessment of CHOL@CDNVs; cytotoxicity assay results; and serum ALT and AST levels. See DOI: https://doi.org/10.1039/d5ra08928j.

Acknowledgements

This work was financially supported by College Student's Innovation and Entrepreneurship Training Program of the Education Department of Guangdong Province (No. S202510576045), Shaoguan Technology Planning Project (No. 230330108034335), Shaoguan University Team Project (No. 2022-27). During the preparation of this work the author(s) used DeepSeek in order to enhance language and readability. After using this tool/service, the author(s) reviewed and edited the content as needed and take(s) full responsibility for the content of the publication.

References

1 L. D. Bos and L. B. Ware, *Lancet*, 2022, **400**, 1145–1156.
2 J. Zhang, Y. Guo, M. Mak and Z. Tao, *J. Transl. Med.*, 2024, **22**, 25.
3 N. J. Meyer, L. Gattinoni and C. S. Calfee, *Lancet*, 2021, **398**, 622–637.
4 C. Liu, K. Xiao and L. Xie, *Front. Immunol.*, 2022, **13**, 971189.
5 R. Vichare and J. M. Janjic, *Inflammation*, 2022, **45**, 2124–2141.
6 F. Hou, N. Shi, H. Yuan, B. Li, J. Xiao, K. Xiao and L. Xie, *Cell. Mol. Biol. Lett.*, 2025, **30**, 69.
7 C. Malainou, S. M. Abdin, N. Lachmann, U. Matt and S. Herold, *J. Clin. Invest.*, 2023, **133**, e170501.
8 H. Aegerter, B. N. Lambrecht and C. V. Jakubzick, *Immunity*, 2022, **55**, 1564–1580.
9 L. Wang, H. Zhang, L. Sun, W. Gao, Y. Xiong, A. Ma, X. Liu, L. Shen, Q. Li and H. Yang, *J. Nanobiotechnol.*, 2020, **18**, 38.
10 Y. Zhao, X. Zhu, L. Hu, F. Hao, X. Ji, X. Hu, M. Luo, L. Zheng, B. Xiao and Y. Wu, *Mater. Today Bio*, 2025, **32**, 101708.
11 C. Liu, R. Zhou, B. Chen, X. Yan, L. Guo, Y. Tang, X. Zuo, X. Guo, H. Yu and J. Chen, *Mater. Today Bio*, 2025, **31**, 101622.
12 R. Liao, Z. Sun, L. Wang, C. Xian, R. Lin, G. Zhuo, H. Wang, Y. Fang, Y. Liu and R. Yang, *Bioact. Mater.*, 2024, **43**, 406–422.
13 L. Liang, W. Peng, A. Qin, J. Zhang, R. Chen, D. Zhou, X. Zhang, N. Zhou, X.-Y. Yu and L. Zhang, *ACS Nano*, 2024, **18**, 21009–21023.
14 J. Yang, X. Huang, Q. Yu, S. Wang, X. Wen, S. Bai, L. Cao, K. Zhang, S. Zhang and X. Wang, *J. Extracell. Vesicles*, 2024, **13**, e12437.
15 A. C. Dixson, T. R. Dawson, D. Di Vizio and A. M. Weaver, *Nat. Rev. Mol. Cell Biol.*, 2023, **24**, 454–476.
16 L. Xia, C. Zhang, N. Lv, Z. Liang, T. Ma, H. Cheng, Y. Xia and L. Shi, *Theranostics*, 2022, **12**, 2928.
17 J. Lin, L. Yang, T. Liu, H. Zhao, Y. Liu, F. Shu, H. Huang, W. Liu, W. Zhang and L. Jiang, *J. Controlled Release*, 2025, **379**, 832–847.
18 K. Lv and Q. Liang, *Front. Immunol.*, 2025, **15**, 1518008.
19 K. Debnath, K. Las Heras, A. Rivera, S. Lenzini and J.-W. Shin, *Nat. Rev. Mater.*, 2023, **8**, 390–402.
20 M. Cao, N. Diao, X. Cai, X. Chen, Y. Xiao, C. Guo, D. Chen and X. Zhang, *Mater. Horiz.*, 2023, **10**, 3879–3894.
21 M. Q. Lian, W. H. Chng, J. Liang, H. Q. Yeo, C. K. Lee, M. Belaid, M. Tollemeto, M. G. Wacker, B. Czarny and G. Pastorin, *J. Extracell. Vesicles*, 2022, **11**, 12283.
22 J. Fu, Z. Liu, Z. Feng, J. Huang, J. Shi, K. Wang, X. Jiang, J. Yang, Y. Ning and F. Lu, *J. Nanobiotechnol.*, 2025, **23**, 270.
23 J. Kim, S. Li, S. Zhang and J. Wang, *Asian J. Pharm. Sci.*, 2022, **17**, 53–69.
24 B. Zhao, H. Lin, X. Jiang, W. Li, Y. Gao, M. Li, Y. Yu, N. Chen and J. Gao, *Theranostics*, 2024, **14**, 4598.
25 L. Ye, Y. Gao, S. W. F. Mok, W. Liao, Y. Wang, C. Chen, L. Yang, J. Zhang and L. Shi, *J. Nanobiotechnol.*, 2024, **22**, 190.
26 H. Ye, C. Li, W. Ye, F. Zeng, F. Liu, F. Wang, Y. Ye, L. Fu and J. Li, in *Common Chinese Materia Medica*, Springer, 2021, vol. 2, pp. 109–184.
27 D. Hao, X. Gu, P. Xiao and Y. Peng, *Chin. Sci. Bull.*, 2013, **58**, 1120–1129.
28 M. Nemati, B. Singh, R. A. Mir, M. Nemati, A. Babaei, M. Ahmadi, Y. Rasmi, A. G. Golezani and J. Rezaie, *Cell Commun. Signaling*, 2022, **20**, 69.
29 Z. Fang and K. Liu, *J. Controlled Release*, 2022, **350**, 389–400.
30 K.-R. Kim, J. Kim, J. H. Back, J. E. Lee and D.-R. Ahn, *ACS Nano*, 2022, **16**, 7331–7343.
31 Y. Zhuo, Z. Luo, Z. Zhu, J. Wang, X. Li, Z. Zhang, C. Guo, B. Wang, D. Nie and Y. Gan, *Nat. Nanotechnol.*, 2024, **19**, 1858–1868.
32 L. Li, M. Zhang, J. Li, T. Liu, Q. Bao, X. Li, J. Long, L. Fu, Z. Zhang and S. Huang, *Nat. Commun.*, 2023, **14**, 5111.
33 W. Gao, Y. Wang, Y. Xiong, L. Sun, L. Wang, K. Wang, H. Y. Lu, A. Bao, S. E. Turvey and Q. Li, *Acta Biomater.*, 2019, **85**, 203–217.

34 Y. Liu, S. Xiao, D. Wang, C. Qin, H. Wei and D. Li, *J. Sep. Sci.*, 2024, **47**, 2300669.
35 P. Li, M. Kaslan, S. H. Lee, J. Yao and Z. Gao, *Theranostics*, 2017, **7**, 789.
36 M. A. Rider, S. N. Hurwitz and D. G. Meckes Jr, *Sci. Rep.*, 2016, **6**, 23978.
37 Y. Chen, J. Xiao, L. Zhang, J. Mu, J. Wang, X. Yu, L. Li, Z. Xiao and Y. Liang, *Int. J. Biol. Macromol.*, 2025, **309**, 142451.
38 X. Guo, X. Zhang, Y. Qi, H. Zhao, S. Du and B. Shao, *Food Chem.*, 2024, **458**, 140219.
39 X. Liu, T. Dong, Y. Zhou, N. Huang and X. Lei, *Angew. Chem., Int. Ed.*, 2016, **55**, 14330–14334.
40 I. Treede, A. Braun, R. Sparla, M. Kühnel, T. Giese, J. R. Turner, E. Anes, H. Kulaksiz, J. Füllekrug and W. Stremmel, *J. Biol. Chem.*, 2007, **282**, 27155–27164.
41 N. Sun, J. Chen, Z. Bao, D. Wang, B. An and S. Lin, *J. Food Sci.*, 2019, **84**, 1002–1011.
42 D. Pozzi, C. Marchini, F. Cardarelli, H. Amenitsch, C. Garulli, A. Bifone and G. Caracciolo, *Biochim. Biophys. Acta, Biomembr.*, 2012, **1818**, 2335–2343.
43 B. G. Tenchov, R. C. MacDonald and D. P. Siegel, *Biophys. J.*, 2006, **91**, 2508–2516.
44 S. Patel, N. Ashwanikumar, E. Robinson, Y. Xia, C. Mihai, J. P. Griffith III, S. Hou, A. A. Esposito, T. Ketova and K. Welsher, *Nat. Commun.*, 2020, **11**, 983.
45 W. Fan, Y. Tang, Y. Liu, Y. Ran, G. Pan, X. Song, L. Mai, X. Jiang, D. Chen and F. Song, *J. Nanobiotechnol.*, 2024, **22**, 729.
46 L. Hou, J. Zhang, Y. Liu, H. Fang, L. Liao, Z. Wang, J. Yuan, X. Wang, J. Sun and B. Tang, *Free Radical Biol. Med.*, 2021, **165**, 219–228.